Proceedings of the
Annual Stability Conference
Structural Stability Research Council
San Antonio, Texas, March 21-24, 2017

Major and Minor Axis Stiffness Reduction of Steel Beam-Columns Under Axial Compression and Tension Conditions

Barry T. Rosson[1]

Abstract

For compact W-Shapes with an ECCS residual stress distribution pattern, the stiffness reduction that results from yielding of the cross-section due to uniaxial bending and axial loading are studied in detail. Major and minor axis bending under axial compression and tension conditions are investigated. Three-dimensional m-p-τ surface plots of a W8x31 are used to discuss the stress states around the perimeter of the surfaces and the reduced stiffness for each of the loading conditions. Figures are provided for the stiffness reduction from initial yield up to the fully plastic conditions for the axial compression and axial tension conditions. The m-p-τ surface plots are used to develop an idealized material model for direct implementation in *MASTAN2*. The El-Zanaty and Kanchanalai benchmark frames are modeled using the new material model. The results compare very closely with published results of the same frames under similar loading conditions. Discussion is provided regarding the proposed material model for practical use.

1. Introduction

The in-plane behavior of steel frames with compact doubly-symmetric beam-columns that are subjected to major and minor axis bending have been shown to exhibit significant differences in their response based on plastic hinge and plastic zone analyses (Attalla 1994; Ziemian et al. 2002). Frames of this type with little to no redundancy can be very sensitive to the refinement of the inelastic analysis procedure employed (White et al. 1991; Ziemian et al. 1997). Recent research has focused on developing improved empirical relationships to account for the reduction in stiffness that occurs due to yielding of the beam-column's cross-section (Zubydan 2011; Kucukler et al. 2014, 2016). The objective of this paper is to present the findings from a detailed fiber element model investigation of the stiffness reduction that develops as a result of yielding in the flanges and web over the full range of moment and axial load combinations from initial yield to the fully plastic condition. Considering both major and minor axis bending under axial compression and tension conditions, analytical expressions are presented to determine the moment and axial load combinations at the initial onset of yielding and when the section becomes fully plastic. Discussion is provided on how the equations can be used to develop an idealized material model for use as tangent modulus values in the nonlinear analysis program *MASTAN2*. The paper discusses how the material model is readily useable for any compact W-Shape and assumed maximum residual stress condition.

[1] Professor, Florida Atlantic University, <rosson@fau.edu>

2. Fiber Element Model

The stiffness reduction (τ) that results from yielding of the cross-section due to bending and axial load was studied in detail for W-Shapes with an ECCS residual stress pattern (1984) as depicted in Fig. 1. For a given normalized moment m (M/M_p), axial load p (P/P_y), and residual stress ratio c_r (σ_r/σ_y), the stiffness reduction was carefully assessed using a detailed fiber element model of a W8x31 with c_r = 0.3. Throughout the paper p is understood to be positive such that the sign on P_y matches that of the applied axial load P. Bending about the minor axis is understood to have a normalized moment $m = M/M_{py}$, and bending about the major axis is understood to have a normalized moment $m = M/M_{px}$.

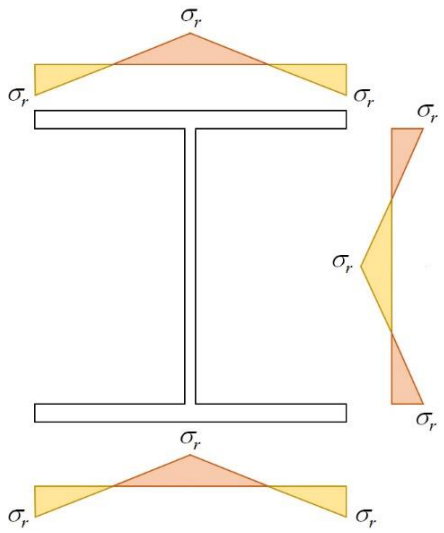

Figure 1: Residual stress pattern used in the study

A computer program was developed to accommodate a specified number of rows and columns of fiber elements in each flange and the web. The angle and location of linear strain distribution were varied in specified increments from zero to specified maximums in order to capture the m and p conditions at 0.01 increments to at least three significant digits of accuracy. The final model used 2,046 fiber elements over the cross-section (400 fiber elements in each flange and 1,246 fiber elements in the web). This level of discretization was found to be necessary to develop the smooth m-p-τ surface plots throughout in the paper.

3. Axial Compression m-p-τ Surface Plots

Using the m and p results with increments of 0.01, over 7,000 data points were used to produce the 3D surface plots (m and p combinations of τ = 0 outside the boundary were excluded). Comparing Fig. 2 with Fig. 3, a triangular shaped plateau of τ = 1 is observed for both minor and major axis bending conditions; however, the 3D surfaces after initial yield vary quite significantly. For the major axis bending condition, the shape of the surface past the initial yield plateau is relatively uniform for p between 0 and 0.7. However, for the minor axis bending condition, the shape is significantly different depending upon the magnitude of p. For the lower values of p with minor axis bending between 0 and approximately 0.2, the loss of stiffness is more gradual for a given increment of m beyond initial yield, and for p between 0.2 and 0.7, the loss of stiffness is more much rapid for the same increment of m. For the higher values of p between 0.7 and 1 with both minor and major axis bending, the surface plots take on a very different shape with a smooth,

distinct fold at values of *m* between 0 and approximately 0.1. For $p > 0.7$, there is a rapid decrease in stiffness to the $\tau = 0$ condition, and as the moment approaches zero, the shape of the curve is convex for minor axis bending and is concave for major axis bending.

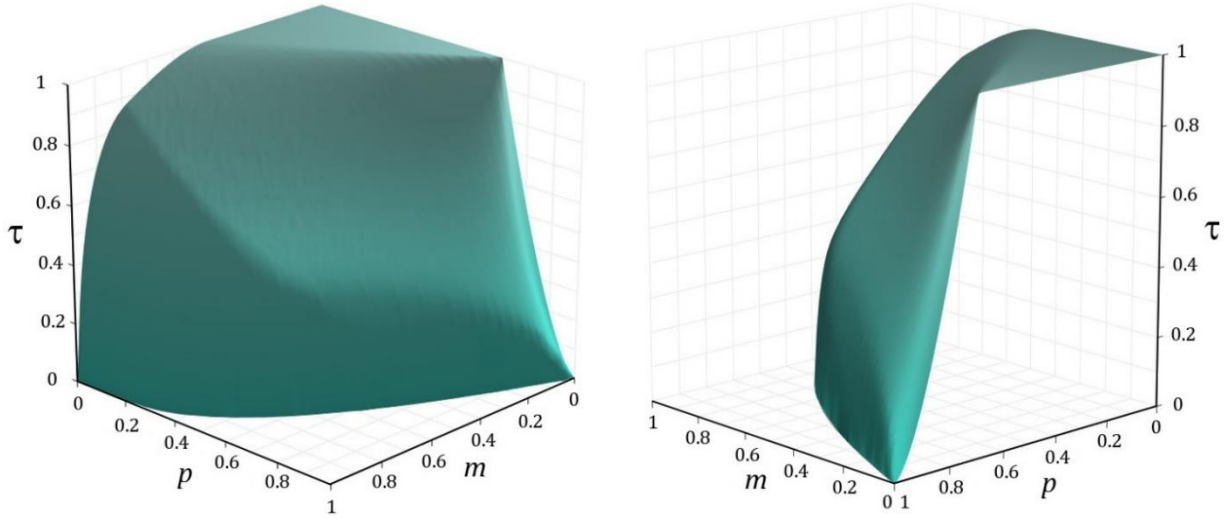

Figure 2: Minor axis bending and axial compression *m*-*p*-τ surface plot

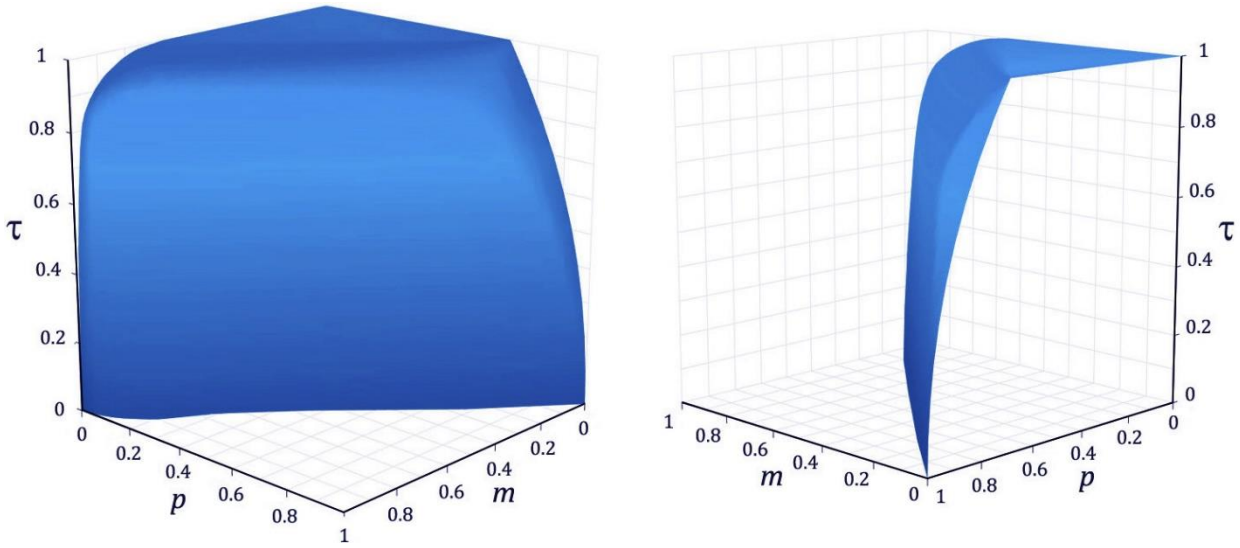

Figure 3: Major axis bending and axial compression *m*-*p*-τ surface plot

As depicted in Figs. 4 and 5, there are four unique conditions around the perimeter of the surface plots. In the following sections of the paper, equations will be given for the lines around the perimeter (except for the blue line). The yellow line indicates the maximum *m* and *p* conditions to maintain an elastic response with $\tau = 1$, and the red line indicates the *m* and *p* conditions for a fully plastic response with $\tau = 0$. The purple line indicates the stiffness reduction under pure compression yield conditions when $p > 1 - c_r$. The blue line requires a number of equations and has been previously published for the minor axis bending condition (Rosson 2016). The major axis bending condition requires a similar number of equations, and as will be discussed later, the blue line in both figures will not be needed to develop the idealized material model.

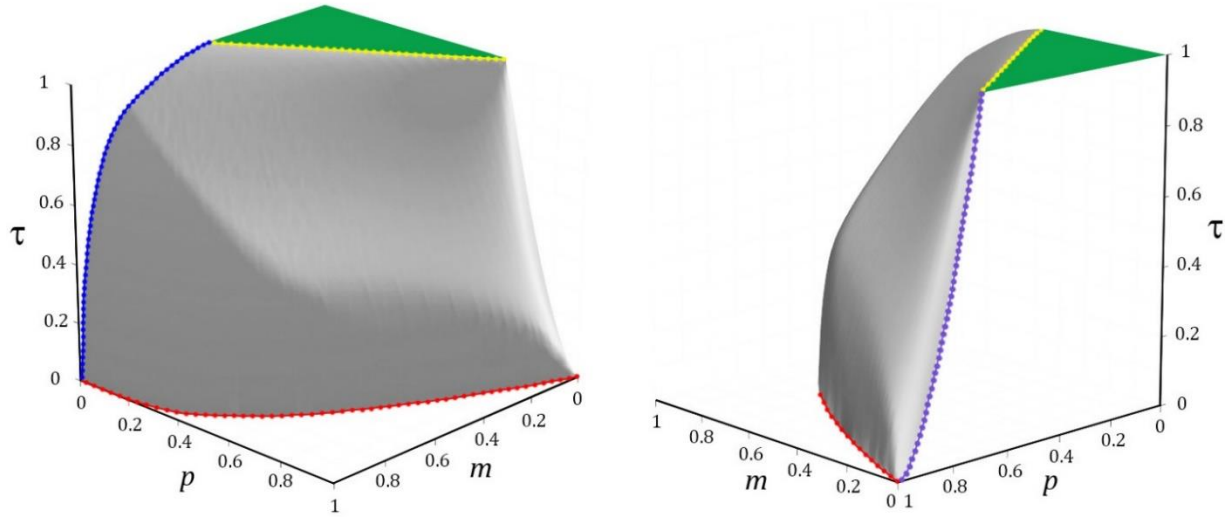

Figure 4: Minor axis bending and axial compression *m*-*p*-τ surface plot perimeter conditions

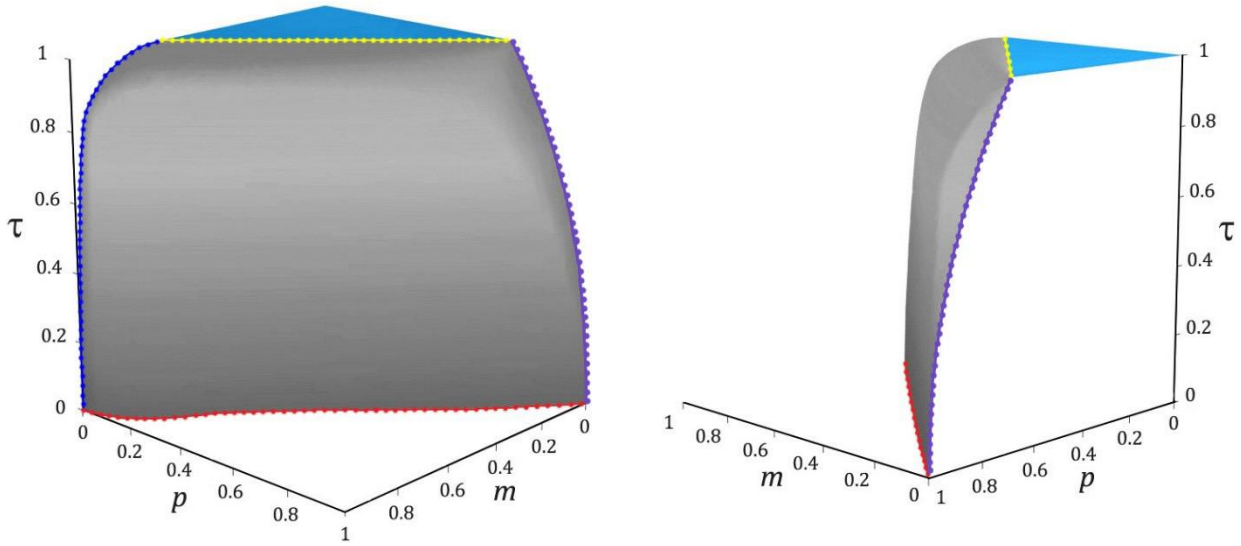

Figure 5: Major axis bending and axial compression *m*-*p*-τ surface plot perimeter conditions

3.1 Yellow line (m and p conditions at the limit of τ = 1)

The equation to determine the extent of τ = 1 is found in the literature (Attalla et al. 1994, Zubydan 2011) and is straight-forward to visualize as depicted in Fig. 6. The dashed blue lines represent the residual stress distribution, and the shaded region represents the final compression stresses across each flange after the bending moment and axial load have been applied. The left side of the diagram depicts the accumulation of three stresses: the residual compression stress σ_r, the bending moment compression stress σ_m, and the axial compression stress σ_p. The extent of τ = 1 is determined when the conditions of *m* and *p* cause all three compression stresses to sum to σ_y. For a given residual stress ratio c_r and axial compression load condition *p*, the maximum moment at which τ = 1 is maintained is given as

$$m_1 = \frac{S_y}{Z_y}(1 - c_r - p) \tag{1}$$

where S_y is the minor axis elastic section modulus and Z_y is the minor axis plastic section modulus. Since this equation is based only on the accumulation of stress at the end of each flange, the assumed shape of the residual pattern does not affect Eq. 1 provided the maximum residual compression stress σ_r occurs at the end of the flanges.

The stresses in the flanges of a W8x31 for c_r = 0.3 and p = 0.5 are given in Fig. 6. Using Eq. 1, compression yielding initiates on the left side when the minor axis bending moment reaches m_1 = 0.132.

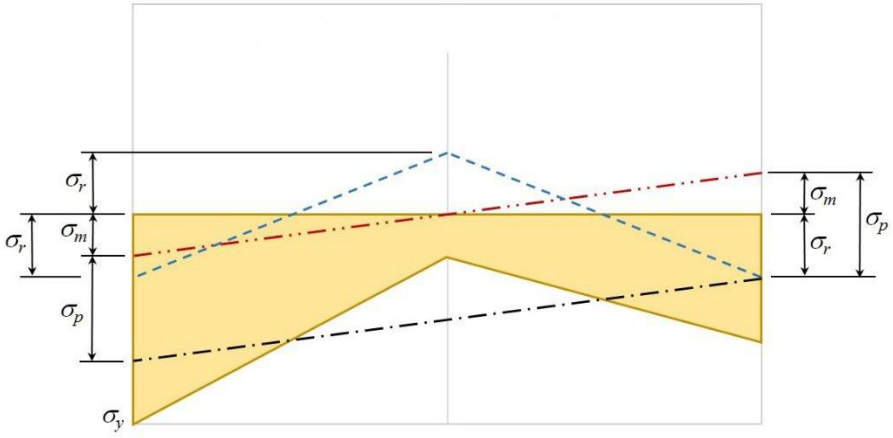

Figure 6: Minor axis bending stress state in the flanges at the extent of τ = 1 for p = 0.5

The maximum moment at which τ = 1 is maintained for major axis bending is determined in a similar manner and is found to be

$$m_1 = \frac{S_x}{Z_x}(1 - c_r - p) \tag{2}$$

where S_x is the major axis elastic section modulus and Z_x is the major axis plastic section modulus. Since this equation is based only on the accumulation of stress at the outer edge of the flange, the assumed shape of the residual pattern does not affect Eq. 2 provided the maximum residual compression stress σ_r occurs at this location.

3.2 Purple line (m = 0 and $p > 1 - c_r$)

The equation to determine the stiffness reduction when m = 0 is found by considering the stress state depicted in Fig. 7. The compressive stress σ_p' that satisfies the equilibrium condition for a given p and c_r condition provides the necessary information to determine the extent of yielding over the length h_y at the ends of the flanges and over the length $2h_y$ at the center of the web. The length h_y is determined using Eq. 3 where $d = b_f$ for yielding in the flanges and $d = d_w$ for yielding in the web.

$$h_y = \frac{d}{2}\left(1 - \sqrt{\frac{1-p}{c_r}}\right) \tag{3}$$

To determine the stiffness reduction τ for a given p and c_r condition, the minor axis moment of inertia of the remaining cross-section that has not yielded is divided by the original minor axis moment of inertia I_y. The relationship for τ is found to be

$$\tau = \frac{2\left(\sqrt{\frac{1-p}{c_r}}\right)^3 + \lambda\lambda_o^2\sqrt{\frac{1-p}{c_r}}}{2 + \lambda\lambda_o^2} \tag{4}$$

where $\lambda = A_w/A_f$ and $\lambda_o = t_w/b_f$. For W-Shapes in which $\lambda\lambda_o^2$ is very small compared to 2, a very close approximation to Eq. 4 excludes the effect of the web and is given as

$$\tau = \left(\sqrt{\frac{1-p}{c_r}}\right)^3 \tag{5}$$

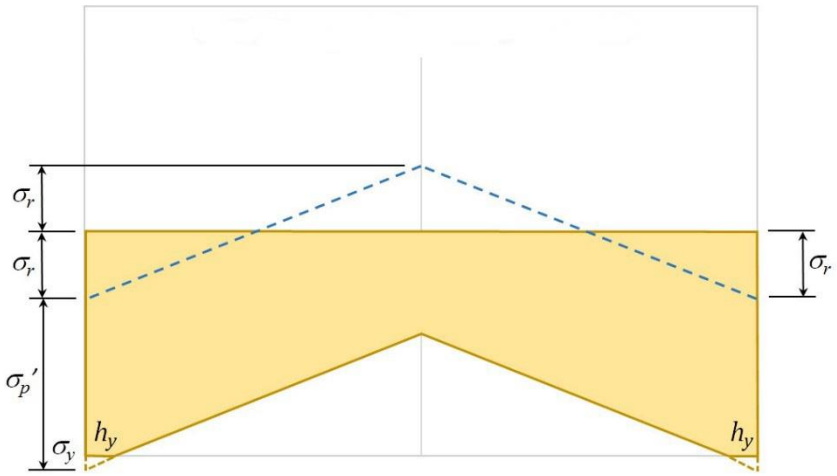

Figure 7: Minor axis bending stress state in the flanges for m = 0 and p = 0.75

The stiffness reduction τ for the major axis condition is determined in a similar manner and is found to be

$$\tau = \frac{\lambda\lambda_1^2\left[1 - \left(1 - \sqrt{\frac{1-p}{c_r}}\right)^3\right] + \sqrt{\frac{1-p}{c_r}}\left[2 + 6(1+\lambda_1)^2\right]}{\lambda\lambda_1^2 + 2 + 6(1+\lambda_1)^2} \tag{6}$$

where $\lambda_1 = d_w/t_f$. Eqs. 4 through 6 are based entirely on the assumed shape of the residual pattern; therefore the shape of the purple lines in Figs. 4 and 5 are unique to the ECCS residual stress pattern given in Fig. 1.

3.3 Red line (m and p conditions for $\tau = 0$)

Two equations are needed to determine the m and p conditions when $\tau = 0$ for both minor and major axis bending. For the minor axis bending condition, one equation is needed when the plastic neutral axis is inside the web thickness, and the other is needed when it is outside the web thickness. Closed-form equations are given in the book by Chen and Sohal (1995); however, the same results can be obtained with fewer computations using the constants λ, λ_o and λ_1.

$$m_0 = 1 - \frac{p^2(2+\lambda)^2}{(2+\lambda\lambda_o)(2+\lambda_1)} \tag{7}$$

$$when\ p \geq \frac{2\lambda_o + \lambda}{2+\lambda} \qquad m_0 = \frac{4 - [p(2+\lambda) - \lambda]^2}{2(2+\lambda\lambda_o)} \tag{8}$$

For the major axis bending condition, one equation is needed when the plastic neutral axis is outside the flange thickness, and the other is needed when it is inside the flange thickness.

$$m_0 = 1 - \frac{p^2(2+\lambda)^2}{4\lambda_o + \lambda(4+\lambda)} \tag{9}$$

$$when\ p \geq \frac{\lambda}{2+\lambda} \qquad m_0 = \frac{(2+\lambda_1)^2 - [p(2+\lambda) - \lambda + \lambda_1]^2}{4 + \lambda_1(4+\lambda)} \tag{10}$$

Eqs. 7 through 10 do not depend upon the assumed shape of the residual pattern; therefore the shape of the red lines in Figs. 4 and 5 are unaffected by the ECCS residual stress pattern.

6. Material Model Idealization of *m-p-τ* Surface Plots

Referring to Figs. 2 and 3, and the equations presented for the yellow, purple and red lines in Figs. 4 and 5, the idealizations in Figs. 8 and 9 were developed for inelastic material model purposes. For both minor axis and major axis bending, the extent of the triangular plateau regions at which $\tau = 1$ is defined by m_1 for a given p condition in Eqs. 1 and 2. Based on the previous discussion concerning the yellow lines, the shape and extent of the plateau regions are relatively independent of the assumed residual stress pattern. Also for both minor axis and major axis bending, the furthest extent of the 3D surfaces at which $\tau = 0$ is defined by m_0 for a given p condition in Eqs. 7 through 10. Based on the previous discussion concerning the red lines, the shape and extent of $\tau = 0$ are independent of the assumed residual stress pattern. When $m = 0$ and $p > 1 - c_r$, Eqs. 4 and 6 were based on the ECCS residual stress pattern, and thus the purple lines were dependent upon the assumed residual stress pattern. Indeed since the fiber element model that was used to develop Figs. 2 and 3 used an ECCS residual stress pattern, the shapes of the 3D surfaces between $\tau = 1$ and $\tau = 0$ are dependent upon the assumed residual stress pattern. Keeping the portions of Figs. 4 and 5 where the actual residual stress distribution has little to no effect, and using a linear variation for τ over the regions where it does have an effect, Fig. 8 was developed for minor axis bending and Fig. 9 for major axis bending. In general, this linearization provides a conservative estimate for τ between the yellow and red lines in Figs. 4 and 5.

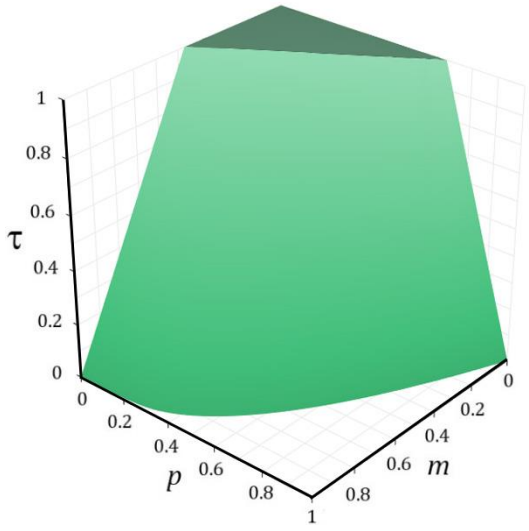

Figure 8: Material model for minor axis bending

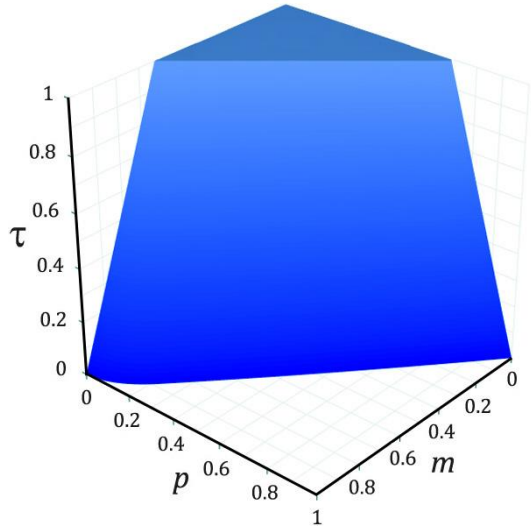

Figure 9: Material model for major axis bending

Using a linear variation in stiffness between the elastic condition of $\tau = 1$ and the fully plastic condition of $\tau = 0$ is also consistent with the approach taken by Ziemian and McGuire (2002) to represent the variation in stiffness in a linear manner over the length of the element. The following two equations are given for the linear variation in stiffness for both minor axis and major axis bending. For a given m and p condition, the stiffness reduction τ can be easily evaluated based on the m_0 and m_1 values from Eqs. 1, 7 and 8 for minor axis bending, and Eqs. 2, 9 and 10 for major axis bending.

$$\tau = \frac{m_0 - m}{m_0 - m_1} \tag{11}$$

$$when\ p \geq 1 - c_r \qquad \tau = \left(\frac{1-p}{c_r}\right)\left(1 - \frac{m}{m_0}\right) \tag{12}$$

Example 1

Determine the stiffness reduction τ of a W8x31 (c_r = 0.3) with minor axis bending m = 0.3 and axial compression load p = 0.6.

λ = 0.5839 $\qquad$ S_y = 9.27 in^3

λ_o = 0.0356 $\qquad$ Z_y = 14.1 in^3

In order to determine τ, first evaluate

$$1 - c_r = 1 - 0.3 = 0.7 \tag{13}$$

Since $p < 0.7$, Eq. 11 will be used, and both m_1 and m_0 will be evaluated.
Eq. 1 is used to obtain m_1.

$$m_1 = \frac{9.27}{14.1}(1 - 0.3 - 0.6) = 0.0657 \tag{14}$$

In order to determine m_0, first evaluate

$$\frac{2\lambda_o + \lambda}{2 + \lambda} = \frac{2(0.0356) + 0.5839}{2 + 0.5839} = 0.254 \tag{15}$$

Since $p > 0.254$, Eq. 8 is used to obtain m_0.

$$m_0 = \frac{4 - [0.6(2 + 0.5839) - 0.5839]^2}{2(2 + 0.5839 \times 0.0356)} = 0.759 \tag{16}$$

Substituting m_1 and m_0 into Eq. 11, the stiffness reduction τ is

$$\tau = \frac{0.759 - 0.3}{0.759 - 0.0657} = 0.66 \tag{17}$$

Example 2

Determine the stiffness reduction τ of a W8x31 (c_r = 0.3) with major axis bending m = 0.2 and axial compression load p = 0.8.

λ = 0.5839 S_x = 27.5 in^3

λ_1 = 16.39 Z_x = 30.4 in^3

Since $p > 0.7$, Eq. 12 will be used, and only m_0 will be evaluated.
In order to determine m_0, first evaluate

$$\frac{\lambda}{2 + \lambda} = \frac{0.5839}{2 + 0.5839} = 0.226 \tag{18}$$

Since $p > 0.226$, Eq. 10 is used to obtain m_0.

$$m_0 = \frac{(2 + 16.39)^2 - [0.8(2 + 0.5839) - 0.5839 + 16.39]^2}{4 + 16.39(4 + 0.5839)} = 0.237 \tag{19}$$

Substituting m_0 into Eq. 12, the stiffness reduction τ is

$$\tau = \left(\frac{1 - 0.8}{0.3}\right)\left(1 - \frac{0.2}{0.237}\right) = 0.10 \tag{20}$$

4. Axial Tension *m*-*p*-τ Surface Plots

Using the same model with 2,046 fiber elements, and the ECCS residual stress pattern with c_r = 0.3, the stiffness reduction for the axial tension condition was studied in the same manner as above. The 3D surfaces in Figs. 10 and 11were developed using m and p increments of 0.01. Comparing Fig. 10 with Fig. 11, the familiar triangular shaped plateau of τ = 1 is observed only for the major axis bending condition; the minor axis bending condition has a more complex plateau region. Comparing Fig. 2 with Fig. 10 for minor axis bending, and Fig. 3 with Fig. 11 for major axis bending, the shape of the 3D surface past the initial yield plateau is similar only for the major axis bending condition. The surfaces are significantly different for minor axis bending under the axial

compression conditions in Fig. 2 versus the axial tension conditions in Fig. 10. The plateau region in Fig. 10 has three distinct ridges and covers a larger area than the plateau region in Fig. 2. The loss of stiffness in Fig. 10 is more gradual for conditions of $p < 0.3$, but for higher values of p the loss of stiffness is more rapid for a given increment of m. For $p > 0.7$, there is a rapid decrease in stiffness to the $\tau = 0$ condition, and as the moment approaches zero, the shape of the curve is convex for both minor axis and major axis bending.

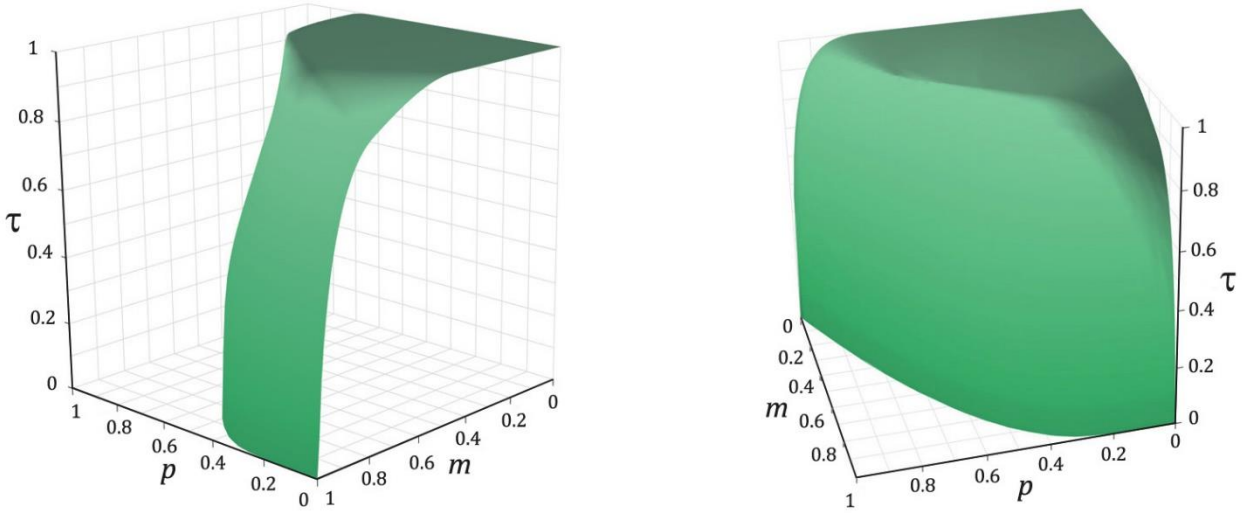

Figure 10: Minor axis bending and axial tension m-p-τ surface plot

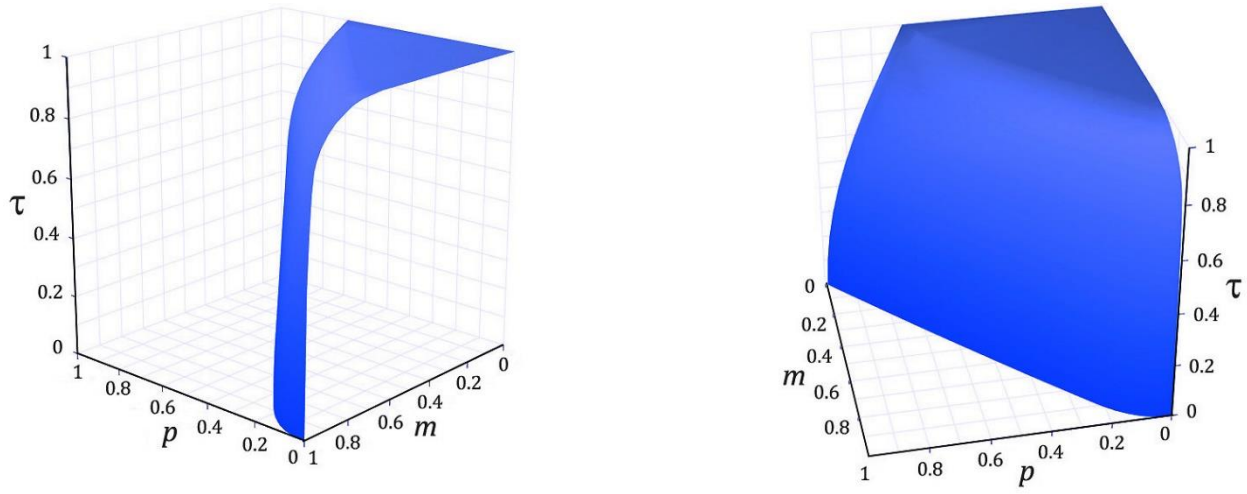

Figure 11: Major axis bending and axial tension m-p-τ surface plot

As depicted in Fig. 12, there are three unique conditions around the perimeter of the plateau for minor axis bending and axial tension conditions. The yellow, magenta and orange lines indicate the maximum m and p conditions to maintain an elastic response with $\tau = 1$, and the red line indicates the m and p conditions for a fully plastic response with $\tau = 0$. The purple line indicates the stiffness reduction under pure tension yield conditions when $p > 1 - c_r$. As before, the blue line requires a number of equations, and it will not be included here due to space limitations.

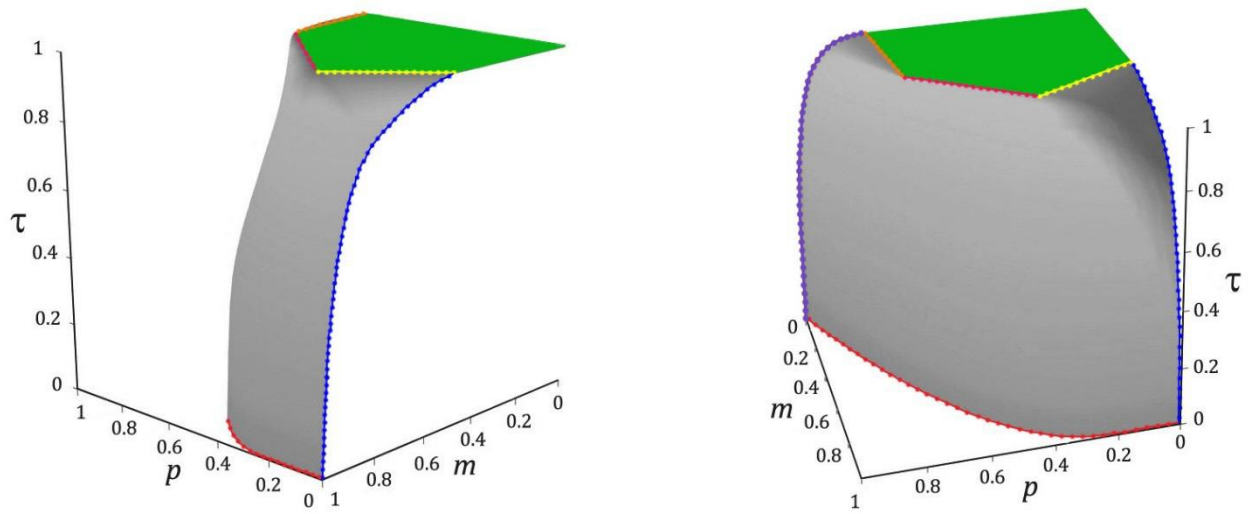

Figure 12: Minor axis bending and axial tension *m-p-τ* surface plot perimeter conditions

4.1 Yellow line with minor axis bending (m and p conditions at the limit of τ = 1)

The first equation of the three where the limit of $\tau = 1$ is reached occurs when compression yielding initiates at the ends of the flanges due to relatively high bending moments and low axial tension conditions. For the axial tension condition $p \leq c_r$, the maximum moment at which $\tau = 1$ is maintained is given as

$$m_1 = \frac{S_y}{Z_y}(1 - c_r + p) \tag{21}$$

4.2 Magenta line with minor axis bending (m and p conditions at the limit of τ = 1)

Under lower bending moments and higher axial tension conditions, the second equation occurs when tension yielding initiates at the ends of the flanges. For the axial tension condition $c_r < p \leq 1 - c_r(1 + \lambda_o)/(1 - \lambda_o)$, the maximum moment at which $\tau = 1$ is maintained is given as

$$m_1 = \frac{S_y}{Z_y}(1 + c_r - p) \tag{22}$$

4.3 Orange line with minor axis bending (m and p conditions at the limit of τ = 1)

Under relatively low bending moments and high axial tension conditions, the third equation occurs when tension yielding initiates in the web at the intersection with the flanges. For the axial tension condition $1 - c_r(1 + \lambda_o)/(1 - \lambda_o) < p \leq 1 - c_r$, the maximum moment at which $\tau = 1$ is maintained is given as

$$m_1 = \frac{S_y}{\lambda_o Z_y}(1 - c_r - p) \tag{23}$$

4.4 Purple line with minor axis bending (m = 0 and p conditions for 0 < τ < 1)

To determine the stiffness reduction τ under pure tension yield conditions, the minor axis moment of inertia of the remaining cross-section that has not yielded is divided by the original minor axis moment of inertia I_y. The shape of the purple line in Fig. 12 is unique to the ECCS residual stress pattern given in Fig. 1. As with Eq. 5, the relationship for τ excluding the effect of the web is given as

$$\tau = 1 - \left(1 - \sqrt{\frac{1-p}{c_r}}\right)^3 \tag{24}$$

4.5 Red line with minor axis bending (m and p conditions for τ = 0)

Two equations are needed to determine the *m* and *p* conditions when τ = 0. Eqs. 7 and 8 derived for the axial compression condition are the same as that for the axial tension condition.

As depicted in Fig. 13, there is only one line at the ridge of the plateau for the major axis bending and axial tension conditions. The yellow line indicates the maximum *m* and *p* conditions to maintain an elastic response with τ = 1, and the red line indicates the *m* and *p* conditions for a fully plastic response with τ = 0. The purple line indicates the stiffness reduction under pure tension yield conditions when $p > 1 - c_r$. As before, the blue line will not be included for the same reasons as previously stated.

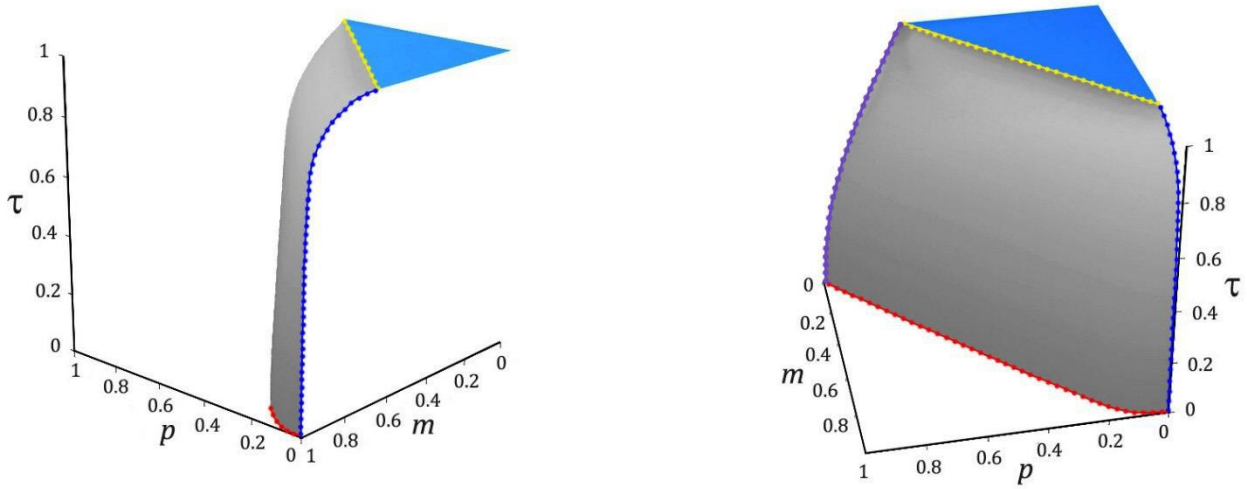

Figure 13: Major axis bending and axial tension *m-p-τ* surface plot perimeter conditions

4.6 Yellow line with major axis bending (m and p conditions at the limit of τ = 1)

This condition occurs when tension yielding initiates at the center edge of the flange. For a given residual stress ratio c_r and axial tension load condition *p*, the maximum moment at which τ = 1 is maintained is given as

$$m_1 = \frac{S_x}{Z_x}(1 - c_r - p) \tag{25}$$

4.7 Purple line with major axis bending (m = 0 and p conditions for 0 < τ < 1)

To determine the stiffness reduction τ for a given p and c_r condition, the major axis moment of inertia of the remaining cross-section that has not yielded is divided by the original major axis moment of inertia I_x. The final expression is similar to Eq. 6 and is given as

$$\tau = \frac{\lambda\lambda_1^2\left(\sqrt{\frac{1-p}{c_r}}\right)^3 + \sqrt{\frac{1-p}{c_r}}[2 + 6(1+\lambda_1)^2]}{\lambda\lambda_1^2 + 2 + 6(1+\lambda_1)^2} \tag{26}$$

4.8 Red line with major axis bending (m and p conditions for τ = 0)

Two equations are needed to determine the m and p conditions when τ = 0. Eqs. 9 and 10 derived for the axial compression condition are the same as that for the axial tension condition.

4.9 Minor axis and major axis bending comparisons

Figs. 14 and 15 illustrate the effects of axial compression versus axial tension on the reduced stiffness using three values of p = 0.2, 0.6 and 0.8. As illustrated in Fig. 14 for a given minor axis bending moment m, the reduced stiffness τ is quite different for the same magnitude of p in compression versus tension. However, as illustrated in Fig. 15, this degree of discrepancy does not exist for the major axis bending condition. As previously mentioned, the shape of the 3D surfaces and the curves in Figs. 14 and 15 are dependent upon the assumed ECCS residual stress pattern. Thus the discrepancies and similarities between the compression and tension results are unique to this assumed residual stress condition. Since the shape of the plateau regions of τ = 1 for both the compression and tension conditions are relatively independent of the residual stress pattern, the discrepancies with the minor axis bending condition and the similarities with the major axis bending condition are predicted to exist for other assumed residual stress patterns.

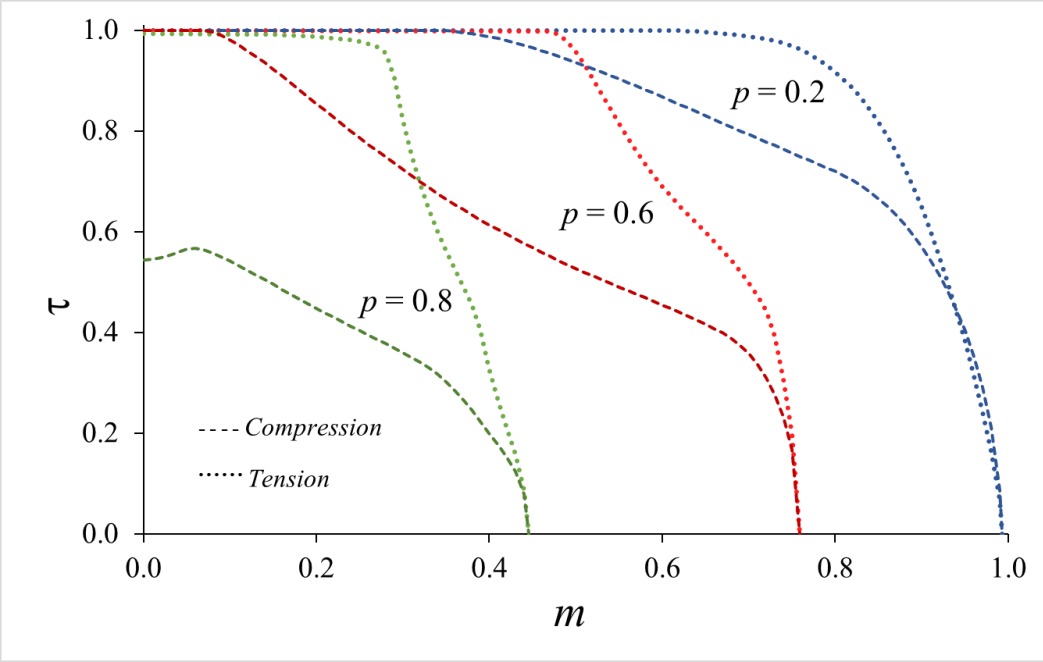

Figure 14: Minor axis bending m-τ curves for p = 0.2, 0.6 and 0.8

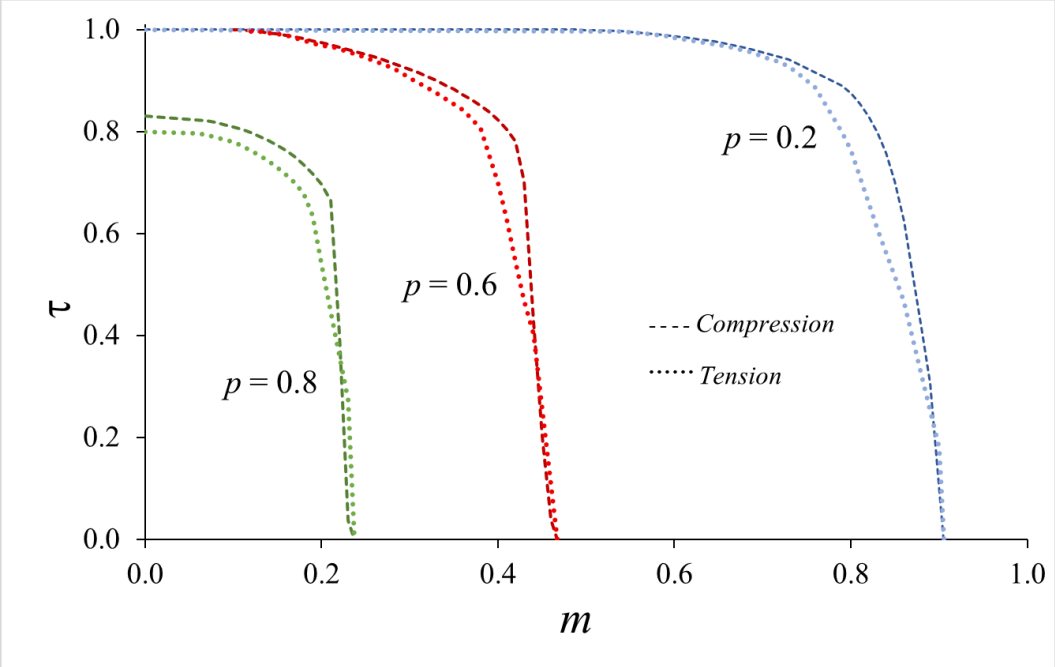

Figure 15: Major axis bending m-τ curves for p = 0.2, 0.6 and 0.8

5. Comparative Examples

The El-Zanaty (1980) and Kanchanalai (1977) benchmark frames have been used by several researchers as comparative examples to test the ability of their method to capture the effects of distributed plasticity on a frame that has little capacity to redistribute forces once yielding has initiated (King et al 1992; Attalla et al 1994; Ziemian et al 2002; Kucukler et al. 2016).

5.1 Stiffness matrix used for modeling the distributed plasticity

Since the bending moments usually vary along the length of the beam-column, the stiffness reduction over the member length must also be accounted for when yielding occurs. An easy and effective way of accomplishing this is to assume the tangent modulus varies linearly over the length of the element. In practice, the error introduced by this assumption is reduced by using multiple elements along the length of the beam-column. The closed-form stiffness matrix developed by Ziemian and McGuire (2002) was chosen for this study because the τ values from Eqs. 11 and 12 can be used directly for the a and b terms in Eq. 27. The tangent modulus is defined to be $E_{tm} = \tau E$. Since the normalized modulus is E_{tm}/E, then $a = \tau$ using the m and p conditions at the start of the element, and $b = \tau$ using the m and p conditions at the end of the element.

$$[k] = \frac{EI_y}{L}\begin{bmatrix} \frac{12}{L^2}\left(\frac{a+b}{2}\right) & -\frac{6}{L}\left(\frac{2a+b}{3}\right) & -\frac{12}{L^2}\left(\frac{a+b}{2}\right) & -\frac{6}{L}\left(\frac{a+2b}{3}\right) \\ & 4\left(\frac{3a+b}{4}\right) & \frac{6}{L}\left(\frac{2a+b}{3}\right) & 2\left(\frac{a+b}{2}\right) \\ & & \frac{12}{L^2}\left(\frac{a+b}{2}\right) & \frac{6}{L}\left(\frac{a+2b}{3}\right) \\ & Sym. & & 4\left(\frac{a+3b}{4}\right) \end{bmatrix} \quad (27)$$

5.2 El-Zanaty portal frame

The stiffness matrix given in Eq. 27 is already a part of the nonlinear material capabilities of *MASTAN2* (2015). The computer program also contains incremental analysis routines for modeling the nonlinear geometric behavior. Eq. 27 with the corresponding τ values from Eqs. 11 and 12 for the W8x31 were used in the nonlinear material subroutine of *MASTAN2*. Eqs. 1 and 2 were used as the limit on the extent of τ = 1, and Eqs. 7 through 10 were used as the boundaries for τ = 0.

The El-Zanaty portal frame as depicted in Fig. 16 was modeled using four elements for all three members. The conditions of p = 0.4 and 0.6 were investigated by first applying the full vertical load P, then the lateral load was applied in increments up to its maximum value of H. The normalized lateral load deflection curves for each condition of p are given in Fig. 16 for both minor axis and major axis bending conditions.

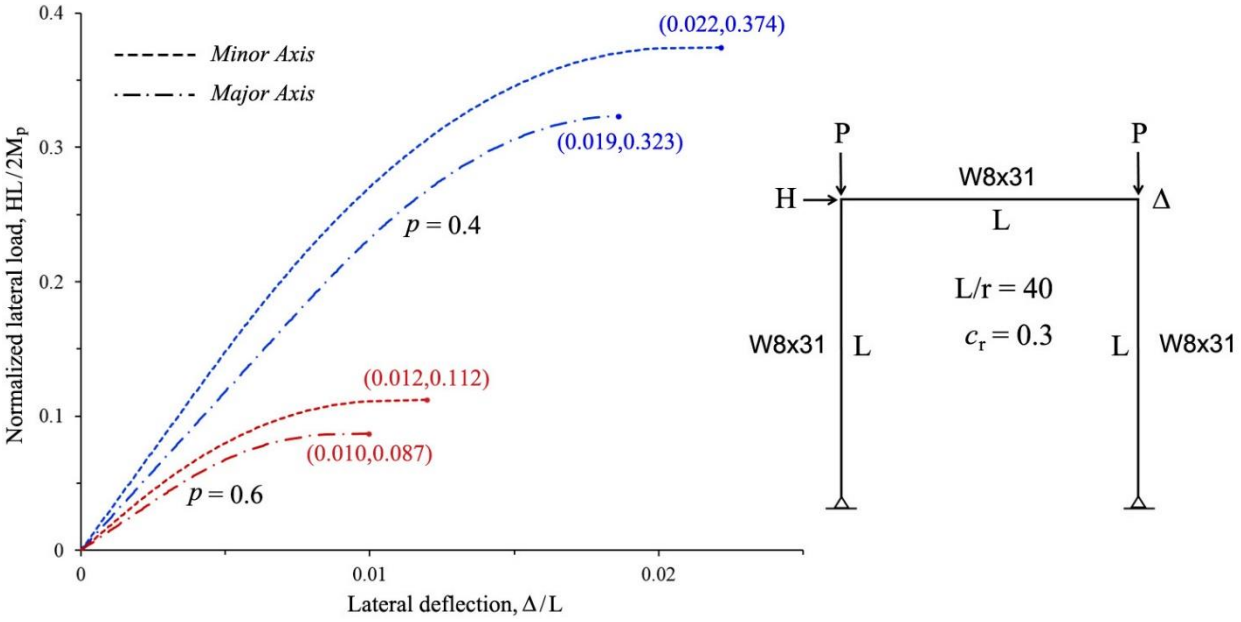

Figure 16: Load deflection curves for El-Zanaty's portal frame with p = 0.4 and 0.6

Table 1: Maximum lateral load and deflection values for El-Zanaty's portal frame

		Minor Axis		Major Axis	
	p	Δ/L	$HL/2M_p$	Δ/L	$HL/2M_p$
Proposed Model	0.4	0.022	0.37	0.019	0.32
	0.6	0.012	0.11	0.010	0.09
Attalla et al. (1994)	0.4	0.020	0.32	0.018	0.32
	0.6	0.006	0.05	0.009	0.10
King et al. (1992)	0.4	n.a.	n.a.	0.018	0.32
	0.6	n.a.	n.a.	0.010	0.11
Ziemian et al. (2002)	0.4	0.020	0.39	n.a.	n.a.
	0.6	0.008	0.09	n.a.	n.a.

n.a. = not available

The maximum lateral load and deflection values for p = 0.4 and 0.6 in Fig. 16 are also presented in Table 1. Comparing the proposed model results with the maximum values from previously published studies of the same frame indicate that the τ values from Eqs. 11 and 12, and the stiffness matrix from Eq. 27, provide a very effective means of modeling the spread of plasticity of frames up to collapse for both minor axis and major axis bending.

5.3 Kanchanalai frame with leaning column

The Kanachanalai leaned frame as depicted in Fig. 17 was modeled using four elements for all three members. The limit load conditions were investigated for both minor axis and major axis bending. The full vertical load P was applied first, then the lateral load H was applied in increments up to its maximum value. The results from analyzing the frame with the proposed material model at six different values of P are compared with Kanachanalai's results. As indicated in Fig. 17, the results compare very closely for both minor axis and major axis bending.

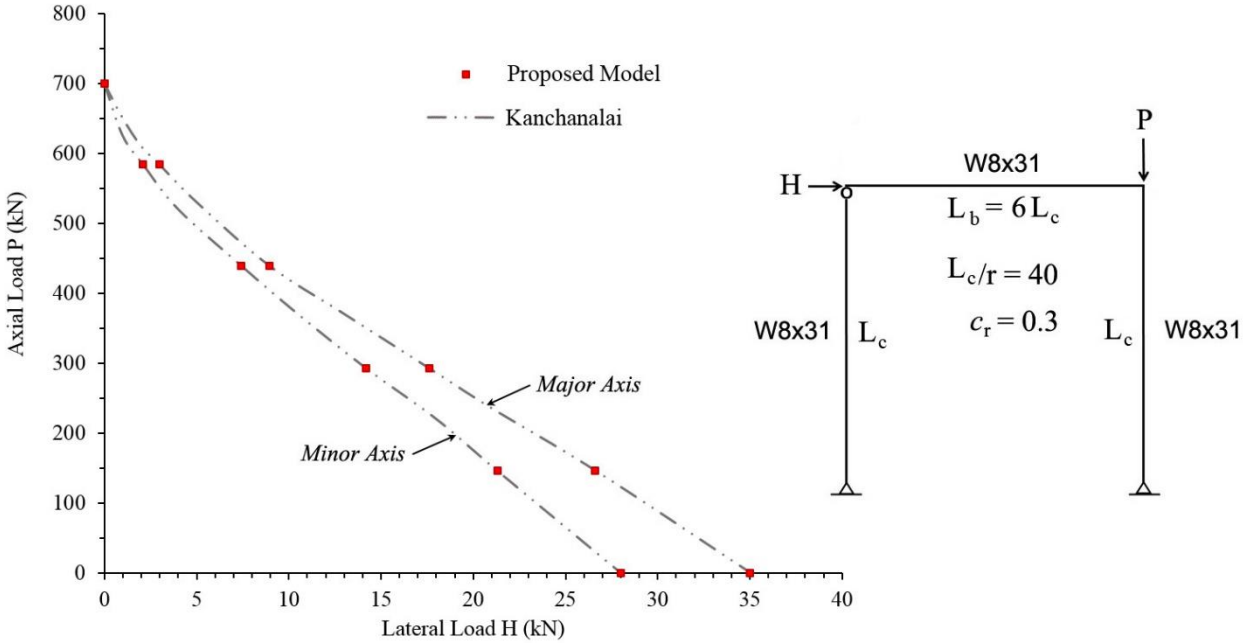

Figure 17: Comparison of proposed model results with Kanchanalai's leaned frame

6. Conclusions

This research focused on developing a deeper understanding of the stiffness reduction that occurs in W-Shapes with an assumed ECCS residual stress pattern and yielding of the cross-section that occurs due to uniaxial bending and axial loading conditions. The study included both minor axis bending and major axis bending, as well as axial compression and axial tension conditions. A detailed model of a W8x31with 2,046 fiber elements and c_r = 0.3 was used to develop three-dimensional m-p-τ surface plots for each condition. The tension condition surface was similar to the compression condition only for major axis bending. For minor axis bending, the shape of the surface was very different between the tension and compression conditions. The m and p conditions around the perimeter of the surfaces were studied in detail and analytical expressions were given for each of the loading conditions at the limit of $\tau = 1$ and $\tau = 0$. The equations for the extent of $\tau = 1$ were found to be dependent only on the location of the maximum residual stresses

and not on the actual distribution of stresses throughout the flanges and web. The equations for $\tau = 0$ are not empirical approximations, but instead they rely upon the actual dimensions of the W-shape.

The m-p-τ surface plots were used as a basis to develop a nonlinear material model for practical use. The shape of the surfaces between $\tau = 1$ and $\tau = 0$ were found to be dependent on the assumed residual stress pattern. Therefore for this reason, and for consistency with the assumed linear variation in stiffness over the length of the element, a linear variation in reduced stiffness over the surface was used for the material model between the initial yield and fully plastic conditions. The material model was used as normalized tangent modulus expressions in *MASTAN2*, and it was found to provide results that were in close agreement with published results for the El-Zanaty and Kanachanalai benchmark frames. The material model is based on reasoning that is consistent with what is known about the effects of the residual stresses in W-shapes. It provides a straightforward and relatively easy to use material model when conducting a nonlinear analysis of planar steel frames with compact W-shapes. Although the paper used a W8x31with $c_r = 0.3$, the material model can accommodate any W-shape and assumed maximum value of residual stress.

References

Attalla M.R., Deierlein G.G., McGuire W. (1994). "Spread of plasticity: quasi-plastic-hinge approach." *Journal of Structural Engineering*, 120 (8) 2451-2473.

Chen W.F., Sohal I. (1995). *Plastic design and second-order analysis of streel frames*. Springer-Verlag, New York.

ECCS (1984). "Ultimate limit state calculation of sway frames with rigid joints." *TC 8 of European Convention for Constructional Steelwork (ECCS)*, No. 33.

El-Zanaty M.H., Murray D.W., Bjorhovde R. (1980). "Inelastic behavior of multistory steel frames." *Structural Engineering Report No. 83*, University of Alberta, Edmonton, Alberta, Canada.

Kanchanalai T. (1977). "The design and behavior of beam-columns in unbraced steel frames." *CESRL Report No. 77-2*, University of Texas, Austin, Texas.

King W.S., White D.W., Chen W.F. (1992). "Second-order inelastic analysis methods for steel-frame design." *Journal of Structural Engineering*, 118 (2) 408-428.

Kucukler M., Gardner L., Macaroni L. (2014). "Stiffness reduction method for the design of steel columns and beam-columns." *Proceedings of the 2014 SSRC Annual Stability Conference*, Toronto, Canada.

Kucukler M., Gardner L., Macaroni L. (2014). "A stiffness reduction method for the in-plane design of structural steel elements." *Engineering Structures*, 73: 72-84.

Kucukler M., Gardner L., Macaroni L. (2016). "Development and assessment of a practical stiffness reduction method for the in-plane design of steel frames." *Journal of Constructional Steel Research*, 126: 187-200.

Rosson B.T. (2016). "Elasto-Plastic Stress States and Reduced Flexural Stiffness of Steel Beam-Columns." *Proceedings of the 2016 SSRC Annual Stability Conference*, Orlando, Florida.

White D.W, Liew Y.J.R., Chen W.F. (1991). "Second-order inelastic analysis for frame design: A report to SSRC Task Group 29 on recent research and the perceived state-of-the-art." *Structural Engineering Report CE-STR-91-12*, Purdue University, West Lafayette, Indiana.

Ziemian R.D., McGuire W. (2002). "Modified tangent modulus approach, a contribution to plastic hinge analysis." *Journal of Structural Engineering*, 128 (10) 1301-1307.

Ziemian R.D., McGuire W. (2015). *MASTAN2*, Version 3.5.

Ziemian R.D., Miller A.R. (1997). "Inelastic analysis and design: frames with members in minor-axis bending." *Journal of Structural Engineering*, 123 (2) 151-156.

Zubydan A.H. (2011). "Inelastic second order analysis of steel frame elements flexed about minor axis." *Engineering Structures*, 33: 1240-1250.